PERGAMON

International Journal of Multiphase Flow 25 (1999) 477–500

International Journal of Multiphase Flow

Force variations on particle induced by bubble-particle collision

T. Hong, L.-S. Fan *, D.J. Lee

Department of Chemical Engineering, The Ohio State University, 140 West 19th Avenue, Columbus, Ohio 43210, USA

Received 8 September 1997; received in revised form 18 August 1998

Abstract

The force variation on a particle during a bubble-particle collision is investigated in two different liquid phases: (1) distilled water and (2) 80 wt% glycerin in water solution. The force variations on a stationary particle due to the collision are experimentally measured and the collision processes are visualized. A simple analytical model of the collision process is developed to account for the pressure force on a particle induced by bubble–particle contact. To obtain physical insight into the bubble–particle collision process, numerical simulations are performed. The computational study agrees closely with the experimental results. Furthermore, the collision between a falling particle and a rising bubble is simulated and compared to the stationary particle case. The simulation of the collision between a bubble and a stationary particle reveals that the force on the particle oscillates: first increases, then decreases, and again increases. The magnitude of the force variation is comparable to the product of the hydrostatic pressure difference across the bubble height and the cross-sectional area of the particle. When the collision takes place in water, the pressure force predominates and the particle experiences both upward and downward forces. When the collision takes place in the glycerin solution, both pressure and viscous forces predominate and the force on the particle induced by the rising bubble is always upward. If a particle is moving downward with a speed relatively faster than that of the rising bubble, the particle experiences an upward drag force due to its downward motion before colliding with a bubble. At the beginning of the collision, the upward force decreases greatly, and recovers quickly. At the end of the collision process, the upward force increases significantly due to the pressure and the wake effect of the bubble. The magnitude of the force variation is comparable to the drag force on the particle before the collision.

Keywords: Bubbly flow; Bubble–particle collision; Numerical simulation; VOF method

* Corresponding author. Tel.: 001 614 292 6591; fax: 001 614 292 3769; e-mail: fan.1@osu.edu

0301-9322/99/$ - see front matter
PII: S0301-9322(98)00056-1

1. Introduction

Three-phase fluidized systems are widely used in chemical and petrochemical industries (Fan, 1989). In a three-phase fluidized bed, bubble-particle interactions and their momentum transfer are key factors contributing to the hydrodynamic behavior of the system. To quantify the momentum transfer due to the bubble-particle interactions, it is necessary to understand the fundamental mechanism underlying the collision process between a bubble and a particle.

Previously, the effect of particles in a gas–liquid system on the bubble size has been investigated extensively by many researchers (Lee, 1965; Ostergaard, 1966; Bruce and Revel-Chion, 1974; Lee et al., 1974; Muroyama and Fan, 1985). Further, studies of the bubble–particle interactions have been carried out both experimentally and analytically (Henriksen and Ostergaard, 1974; Chen and Fan, 1989a; Chen and Fan, 1989b). These studies emphasized the mechanism of bubble breakage due to the particle collision.

Since the bubble–particle collision is not only an extremely rapid transient process, but also involves a very small force variation, it is experimentally challenging to quantify the force experienced by the particle during the collision process. An experimental method using an atomic force microscope has been developed by many researchers (Ducker et al., 1990; Lin et al., 1993; Tsao et al., 1993; Butt, 1994). An atomic force microscope can be used to measure a very small force encountered in the particle; however, it is difficult to measure the force in rapid transient variations, such as the process of bubble–particle collision in liquid. Computational fluid dynamics can be used to quantify the force in such a rapid transient process. A computational study can provide the evolution of the detailed pressure and velocity fields around the bubble and the particle, thereby revealing physical insights into the collision process.

In the present study, the force variation on a particle during a bubble–particle collision is studied experimentally and analytically. Furthermore, numerical simulations are performed to investigate the collision process under various conditions. Results from the analytical model and the numerical simulation are compared with the experimental data. Physical mechanisms underlying the bubble–particle collision process are discussed in light of the numerical simulation.

2. Experimental setup

2.1. Experimental setup

A schematic diagram of the experimental apparatus is shown in Fig. 1. Experiments are performed in a 15.24 cm ID cylindrical Plexiglas column. Two solutions are used as the liquid phase to investigate the viscosity effect: (1) distilled water and (2) 80 wt% glycerin solution with distilled water. The fluid viscosity is measured by a rotational viscometer (Fann series 35 viscometer). Spherical particles of 0.95 and 0.635 cm in diameter are used for the cases of water and of the glycerin solution, respectively. The same size bubble of 1.2 cm in volume equivalent diameter is injected for both cases. A video system with a recording speed of up to 240 pictures per s is employed to record the collision process.

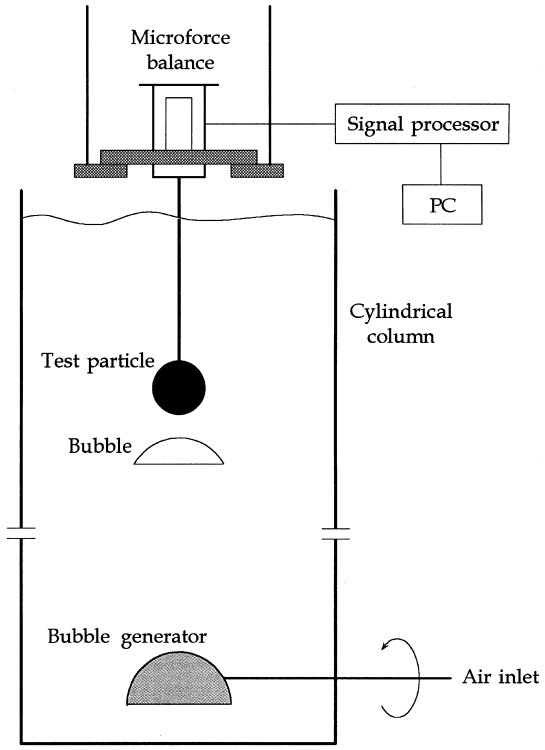

Fig. 1. Schematic description of the experimental apparatus.

A microforce measurement system used by Zhu et al. (1994) is adopted in this study to measure the force variation during the bubble–particle collision process. The particle is connected to an electronic balance (Scientech, Model 202-004) through a rigid thin rod to measure the force acting on the particle. The electronic balance has a sensitivity of 1 mg. The analog output is converted to a digital signal through an A/D converter with 16-bit resolution (National Instruments Data Acquisition Board, AT-MIO-16x) and is recorded by a PC. The data sampling frequency of 3000 Hz is used throughout the experiments. It should be noted that the frequency used in the experiment is higher than the manufacturer-suggested maximum sampling frequency of the electronic balance. A great difficulty was encountered in searching for a microforce balance with both high precision and short response time, and, as a compromise, the present electronic balance is used. The net force on the particle is obtained by subtracting the gravitational and buoyancy contributions from the total force measured by the balance. The gravitational and buoyancy contributions are predetermined in the stationary fluid.

A hemispherical cup of 2 cm in diameter is used to generate a single bubble (Kumar et al., 1992). Air is injected beneath the cup, which is located 5 cm above the bottom of the column, through a stainless steel tube using a syringe to obtain precise volume control. A single bubble is then generated by inverting the cup and releasing the trapped air. This single bubble generation system keeps the disturbance in the flow field minimal and prevents satellite bubble

generation. The distance between the cup and the particle is great enough to nullify any effect of the bubble generation process on the bubble–particle collision.

2.2. Results and discussion

Define F as the net force on the particle in the direction opposite to gravity after the deduction of both the gravitational and the buoyancy forces. Fig. 2 shows the variation of F vs time during the bubble–particle collision in distilled water. It is found that in water the impact process on the particle can be divided into three stages: (1) an upward force in the early stage, (2) a downward force in the middle stage, and (3) an upward force again at the late stage. Fig. 3 shows the variation of F vs time in the case of 80 wt% glycerin solution. In contrast to the case of water, it is observed in Fig. 3 that there is no downward force during the collision process. There is a significant increase in F at the early stage of the collision in the case of the glycerin solution, followed by a decrease, and then another increase that lasts for a prolonged time.

The result reveals a unique time variation of F during the bubble–particle collision process. However, the experimental study alone is insufficient to reveal precise quantitative results of F during the collision process since both the force involved in the collision and the duration of the force are very small. For the particle diameter, d_p, and the volume equivalent bubble diameter, d_b, at around 1 cm, the force involved during the collision is only on the order of one hundred dynes. For such a small force, the microforce balance gives a poor signal to noise

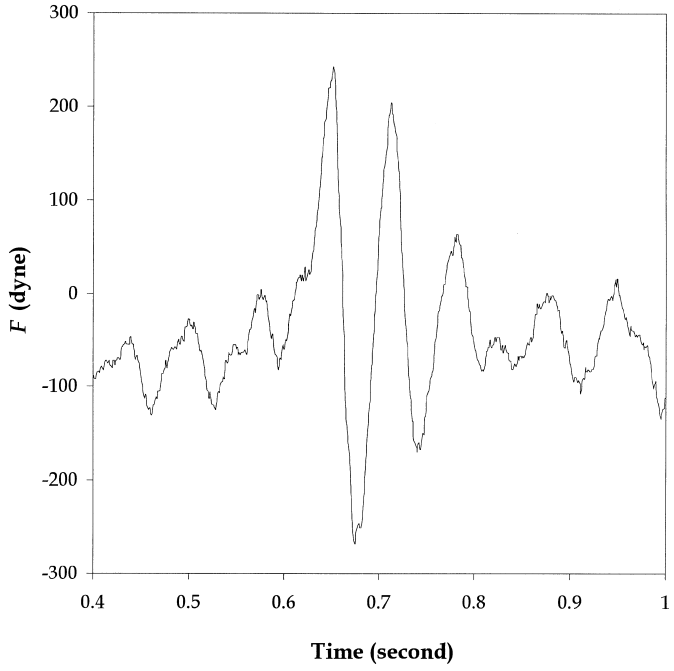

Fig. 2. Experimentally obtained force variation on a particle ($d_p = 0.95$ cm) during the collision with a bubble ($d_b = 1.2$ cm) in distilled water.

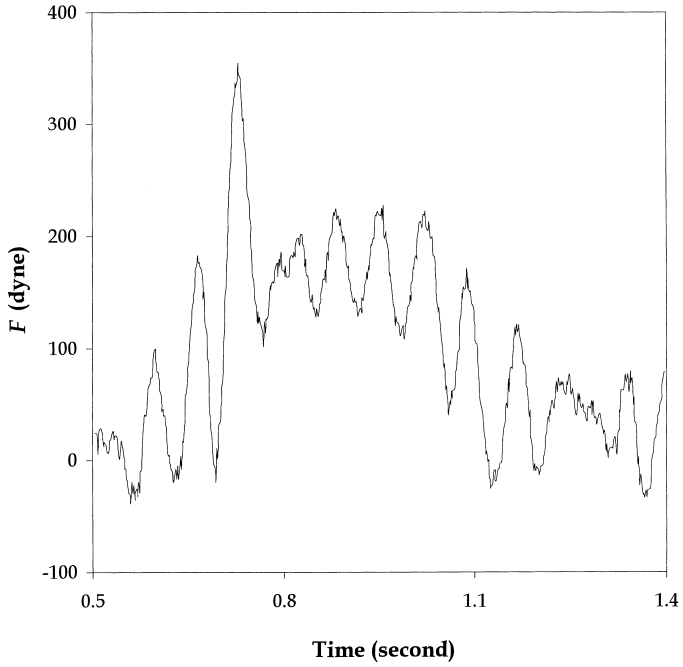

Fig. 3. Experimentally obtained force variation on a particle ($d_p = 0.635$ cm) during the collision with a bubble ($d_b = 1.2$ cm) in 80 wt% glycerin solution.

ratio. Moreover, the collision lasts only a fraction of a second for these particle and bubble sizes, which results in very steep slopes in the force variation. In order to obtain a better understanding of the collision process, a simple analytical model is developed.

3. Analytical study

3.1. Model formulation

The following assumptions are made in this analytical model: (1) the center of the particle is fixed in space located on the central axis of the column, and the center of the bubble moves along the central axis throughout the collision process. (2) The bubble reaches its terminal velocity and is of spherical-cap shape. Further, the bubble rise velocity and the bubble shape, which are determined from the empirical correlations (Fan and Tsuchiya, 1990), remain the same throughout the collision process. (3) The fluid motion induced by the bubble motion and the bubble–particle collision is negligible; thus, the particle experiences neither a pressure force nor a friction force due to the liquid motion. (4) A hydrostatic pressure field is induced by the gravitational force, and the particle only experiences the pressure force during the collision. (5) The pressure inside the bubble is uniform, and is equal to the hydrostatic pressure at the bottom of the bubble. (6) The pressure on the bubble–particle contact area is equal to the

pressure inside the bubble. (7) A thin liquid film covers the particle during the collision; thus, the surface tension force is neglected.

The pressure variation induced by the gravitational force inside the bubble is negligible because the density of water is approximately one thousand times larger than that of air; thus, the pressure inside the bubble is assumed to be uniform as stated in Assumption (5). There is no pressure difference across the flat interface, i.e. the pressure in the gas phase is equal to the pressure in the liquid phase across the gas–liquid interface on the flat bottom of the spherical-cap bubble as noted in Assumption (5). Further, it is assumed that a thin liquid film covers the particle surface throughout the collision process because the dynamic contact angle on the particle surface approaches zero degrees as the relative motion between the bubble and the particle during the collision is very fast (Elliott and Riddiford, 1967).

Fig. 4 shows a schematic diagram of a bubble surrounding the middle portion of a particle. The z-axis indicates the central axis of the column, and the direction of the gravitational acceleration, g, is in the negative z direction. The point O is the center of the spherical particle. Assuming the hydrostatic pressure to be zero at point O, the liquid pressure, p, on the particle surface, except the surface area surrounded by the bubble, can be expressed as

$$p = p(\alpha) = \rho g r_{\mathrm{p}} \cos\alpha \tag{1}$$

where ρ is the fluid density; r_{p} is the particle radius; and α is the angle measured from the reverse direction of the central axis. Because of the axisymmetric nature of the system, there is no horizontal component in the net force. The differential force, $\mathrm{d}F$, in the vertical direction can be expressed as

$$\mathrm{d}F = p(\alpha)\cos\alpha\,\mathrm{d}s \tag{2}$$

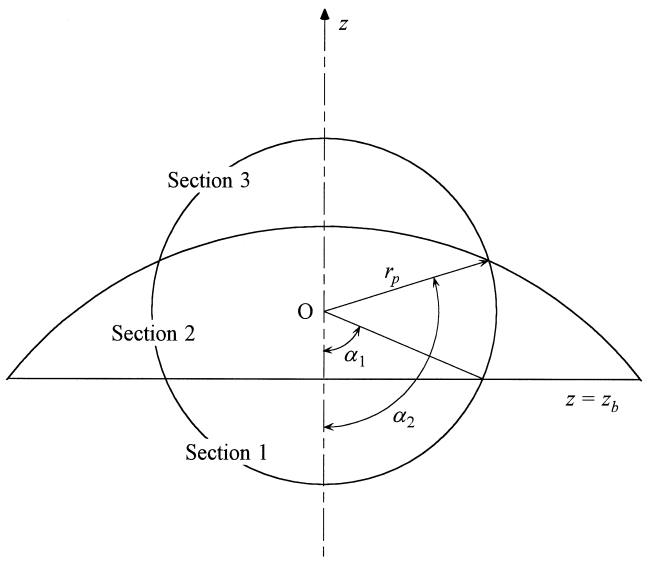

Fig. 4. Schematic description of geometric relationships for the analytical model.

where ds is the band-shaped differential surface area of the particle, and can be expressed as

$$\mathrm{d}s = 2\pi r_\mathrm{p}^2 \sin\alpha \,\mathrm{d}\alpha. \tag{3}$$

The particle surface is divided into three sections, above, within, and beneath the bubble, as shown in Fig. 4. The net force on the particle, F, is the combined effect of the three forces F_1, F_2, and F_3 acting on the three sections of the particle surface. The force on each section of the particle surface can be obtained by integrating Eq. (2) over the corresponding particle surface area. F_1 and F_3 can be obtained from

$$F_1 \int_0^{\alpha_1} (\rho g r_\mathrm{p} \cos\alpha)\cos\alpha(2\pi r_\mathrm{p}^2 \sin\alpha \,\mathrm{d}\alpha) = -\frac{2}{3}\pi r_\mathrm{p}^3 \rho g(\cos^3\alpha_1 - 1) \tag{4}$$

and

$$F_3 = \int_{\alpha_2}^{\pi} (\rho g r_\mathrm{p} \cos\alpha)\cos\alpha(2\pi r_\mathrm{p}^2 \sin\alpha \,\mathrm{d}\,\alpha) = \frac{2}{3}\pi r_\mathrm{p}^3 \rho g(1 + \cos^3\alpha_2) \tag{5}$$

where α_1 and α_2 are determined by the junction of the bubble and the particle. Based on Assumption (5), the pressure on the particle surface in Section 2 (see Fig. 4) can be determined by the horizontal level at the bottom of the bubble, z_b

$$F_2 = \int_{\alpha_1}^{\alpha_2} (\rho g z_\mathrm{b})\cos\alpha(2\pi r_\mathrm{p}^2 \sin\alpha \,\mathrm{d}\,\alpha) = \pi r_\mathrm{p}^2 \rho g z_\mathrm{b}(\sin^2\alpha_2 - \sin^2\alpha_1). \tag{6}$$

Summation of Eqs. (4)–(6) yields

$$F_1 + F_2 + F_3 = \pi r_\mathrm{p}^2 \rho g\left[z_\mathrm{b}(\sin^2\alpha_2 - \sin^2\alpha_1) - \frac{2}{3} r_\mathrm{p}(\cos^3\alpha_1 - \cos^3\alpha_2 - 2)\right]. \tag{7}$$

Finally, after the subtraction of the buoyancy force from Eq. (7), F can be written as

$$F = \pi r_\mathrm{p}^2 \rho g\left[z_\mathrm{b}(\sin^2\alpha_2 - \sin^2\alpha_1) - \frac{2}{3} r_\mathrm{p}(\cos^3\alpha_1 - \cos^3\alpha_2)\right]. \tag{8}$$

For a given z_b, based on Assumption (2), α_1 and α_2 can be determined from the geometrical relations in Fig. 4; therefore, F is only a function of z_b for a fixed system. Note that z_b can be calculated from the bubble rise velocity and time as

$$z_\mathrm{b} = v_\mathrm{b} t \tag{9}$$

where v_b is the bubble rise velocity that can be determined from empirical correlation, e.g. Fan and Tsuchiya (1990).

3.2. Results and discussion

For the case of water ($d_\mathrm{p} = 0.95$ cm and $d_\mathrm{b} = 1.2$ cm), the force variation is obtained by Eq. (8). The aspect ratio of a spherical-cap bubble and the bubble rise velocity is taken to be 0.24 (Vakhrushev and Efremov, 1970) and 25 cm/s (Fan and Tsuchiya, 1990),

respectively. Fig. 5 shows both the predicted and experimental results. The predicted force variation closely follows the experimental result for the case of water except at the last stage of the collision.

The force variation shown in Fig. 5 can be explained as follows. The hydrostatic pressure at any point is determined by the corresponding z, and increases as the corresponding z decreases. From Assumption (5), the pressure inside the bubble, p_b, is higher than its surrounding liquid pressure except at the bottom of the bubble where p_b is equal to the liquid pressure. Therefore, the bubble is a high-pressure zone compared with its surrounding liquid. When the bubble passes around the particle, the pressure on the particle surface surrounded by the bubble increases to p_b. Meanwhile, from Assumption (3), the pressure distribution on the rest of the particle surface remains unchanged, and is equal to the hydrostatic pressure distribution.

At the beginning of the collision, the bottom portion of the particle first touches the bubble, and the increase of the pressure on the bubble–particle contact area results in an upward force on the particle. As the bubble rises, the bubble–particle contact area increases, which leads to a continuous increase in the upward force. Just before the particle penetrates the bubble, the upward force reaches a maximum. After the bottom of the particle is exposed to the liquid, the bubble–particle contact area gradually shifts to the sides of the particle. As a consequence, the upward force begins to decrease. As the bubble moves to the upper portion of the particle, the high pressure on the bubble–particle contact area begins to push the particle downward. As the bubble covers the entire top region of the particle, the downward force reaches a

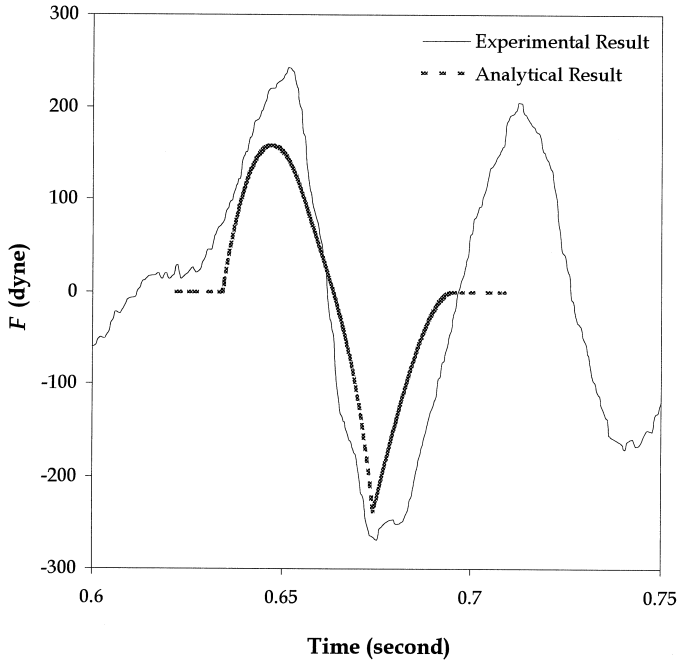

Fig. 5. Analytical and experimental results of the force variation on a particle ($d_p = 0.95$ cm) during the collision with a bubble ($d_b = 1.2$ cm) in water.

maximum. As the bubble rises away from the particle, the bubble–particle contact area shrinks; thus, the downward force gradually decreases to zero when the bubble separates from the particle. Fig. 5 shows that the magnitude of the variation of F is about twice that of the product of the cross-sectional area of the particle and the hydrostatic pressure difference based on the bubble height.

Although the analytical study provides helpful insights into the collision process, a comparison with the experimental result (Fig. 5) shows that the amplitude of the predicted force variation is smaller than that of the experimental result. Further, the experimental result shows another upward force at the late stage of the collision process. The deformation of the bubble shape and the effect of the liquid motion play a significant role on F during the collision process that is neglected in the analytical model.

Fig. 6 shows the force variations obtained experimentally and analytically in the glycerin solution (using the aspect ratio of 0.24 and the bubble rise velocity of 23.6 cm/s). As shown in the figure, the experimentally measured upward force is much larger than the analytical prediction. There is no downward force during the entire collision process and the collision process lasts much longer than predicted. In general, the analytical prediction oversimplifies the force variation behavior in the highly viscous liquid. To fully understand the behavior of F variation during the bubble–particle collision, a comprehensive numerical simulation is to be performed, which accounts for the pressure force, the viscous force, and the effects of the fluid motion and the bubble deformation.

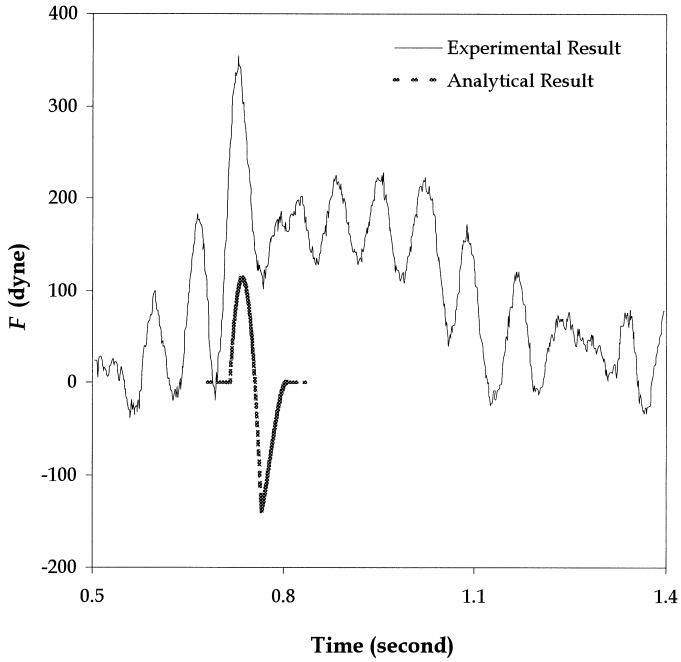

Fig. 6. Analytical and experimental results of the force variation on a particle ($d_p = 0.635$ cm) during the collision with a bubble ($d_b = 1.2$ cm) in 80 wt% glycerin solution.

4. Numerical study

4.1. Numerical method

The successful tracking of the gas–liquid interface is crucial to a numerical study of the system because the physical properties change drastically between phases. The volume of fluid (VOF) method (Hirt and Nichols, 1981) is used in this study, which provides a simple and economical technique to track the gas–liquid interface with reasonable accuracy and a relatively small computer memory requirement. The VOF method has been successfully used to predict the characteristics of single bubble rise, bubble and bubble–chain formation, and bubble breakage (Tomiyama et al., 1993; Bugg and Rowe, 1993; Gracia-Briones et al., 1994; Hong et al., 1996; Deitz, 1998). By tracking the movement of the gas–liquid interface, the VOF method determines the location, the shape, the volume, and the inside pressure of the bubble. No assumptions are made on the gas–liquid momentum transfer. The interaction is directly simulated by changing the pressure distribution induced by the motion of the gas–liquid interface. The factors affecting the gas–liquid interaction, such as surface tension and viscosity, can be directly investigated. It should be noted that the computational grid has to be very fine to provide sufficient cells to represent the bubble when using the VOF method.

4.1.1. Motion of liquid phase

In this computation, the Navier–Stokes equations are solved for the transient laminar incompressible flow. The continuity and the momentum equation of the liquid are

$$\nabla \cdot \mathbf{U} = 0, \tag{10}$$

$$\frac{\partial \rho \mathbf{U}}{\partial t} + \nabla \cdot (\rho \mathbf{U}\mathbf{U}) = -\nabla p + \mu \nabla^2 \mathbf{U} + \rho g, \tag{11}$$

where $\mathbf{U}$ is the velocity vector, t is time, and μ is the viscosity. Eq. (11) is solved to provide the velocity field and the pressure distribution of the liquid phase.

4.1.2. Motion of bubble (gas–liquid interface)

Defining f as the volume fraction of the liquid phase in a computational cell, f is equal to one or zero if the liquid phase or the bubble, respectively, occupies the cell. Hence, the gas–liquid interface can only exist in a cell in which f lies between zero and one. In the VOF method, the movement of the gas–liquid interface is tracked as the f distribution changes. From the mass conservation of the liquid phase, the time-dependent governing equation of f can be obtained as

$$\frac{\partial f}{\partial t} = -\mathbf{U} \cdot \nabla f. \tag{12}$$

At each time increment, the liquid velocity field is computed. Eq. (12) is then used to update the f distribution. The new location and shape of the gas–liquid interface are determined from the renewed f distribution.

Since the density of the liquid is a thousand times larger than that of the gas, the momentum of the liquid phase is much higher than the gas momentum; thus, the gas motion inside the bubble is neglected in this study. Furthermore, because the liquid viscosity is much larger than that of the gas phase, it is assumed the friction drag on the gas–liquid interface is negligible; thus, there is no liquid velocity gradient on the bubble surface. The bubble deformation process is assumed to be isentropic (Champman and Plesset, 1971; Jensen, 1974), so that the pressure inside the bubble can be related to its volume, v, by

$$p_b v^{\gamma} = \text{constant} \tag{13}$$

where γ is the ratio of the specific heats of air and is equal to 1.4.

Based on the bubble shape obtained from the f distribution, the surface curvature at any point on the bubble surface can be determined. Thus, the pressure difference across the gas–liquid interface, Δp, can be obtained from the Laplace–Young equation,

$$\Delta p = \frac{2\sigma}{R} \tag{14}$$

where σ is the surface tension of the liquid phase and R is the radius of the bubble surface curvature at a given point. From Eqs. (13) and (14), the pressure distribution on the liquid side along the bubble surface is determined and then used as the boundary condition for solving liquid momentum equations, Eq. (11), at the next time increment. Again, the f distribution, the shape, the volume, and the pressure of the bubble can then be obtained from the new liquid flow field.

Given the pressure distribution and the velocity field around the particle, the total force on the particle, **F**, consisting of both pressure and viscous forces, can be obtained from

$$\mathbf{F} = \oint_s -p\mathbf{n} \cdot \mathbf{i}\, \mathrm{d}s + \oint_s \mu \frac{\partial \mathbf{U}}{\partial \mathbf{n}} \cdot \mathbf{i}\, \mathrm{d}s \tag{15}$$

where **i** is oriented normal to the particle surface.

4.1.3. Boundary and initial conditions

A non-slip boundary condition is used at the particle surface and at the column wall. An axisymmetric condition is used at the central axis. Initially, the liquid phase is motionless and the pressure distribution is the hydrostatic pressure field induced by the gravitational field. The bubble is assumed to be of spherical shape, and p_b is assumed to be equal to the liquid hydrostatic pressure at the center of the bubble. The parameters used in the numerical simulations are given in Table 1. As discussed above, it is assumed that a thin liquid film covers the particle throughout the collision. This assumption is applied in the simulation by using a 90° contact angle at the particle surface, α_c, and assuming there is no surface tension force along the particle-bubble contact line.

4.1.4. Numerical arrangement

The center of the bubble rises along the central axis of the column toward the center of the particle, and the bubble and the flow are axisymmetric throughout the collision process. The spherical-shaped particle is motionless or moves along the central axis of the column at a

Table 1
Parameters used in the numerical simulation

	ρ (g/cm^3)	μ (g/cm-s)	g (cm/s^2)	σ (dyne/cm)	α_c
Glycerin solution	1.206	0.529	980	65.9	90°
Distilled water	1.0	0.01	980	72.0	90°

constant velocity throughout the collision process. The conservation equations are written in cylindrical coordinates, and an axisymmetric profile of the cylindrical column is used as the computational domain. The dimension of the grid is 33×100.

The finite difference method is used to solve the governing equations. The algorithm is similar to that in the SOLA code (Hirt et al., 1975). The computation is performed on a CRAY Y-MP8/864 supercomputer at the Ohio Supercomputer Center using the fluid dynamics solver FLOW-3D developed by Flow Science, Inc. (Harper et al., 1991). It is noted that when using the time marching algorithm, the time increment needs to be very small to correctly simulate the physical process; hence, a large amount of computational time is involved. In the present study, the time step is on the order of 10^{-4} s which results in the computational time of about 10 CRAY CPU h for a typical case study.

4.1.5. Code verification

An air bubble rising at its terminal velocity is simulated. As shown in Table 2, cases (a) and (b) represent studies in 80 wt% glycerin solution and in distilled water, respectively. In both cases, the bubble shape and the flow field are assumed to be axisymmetric, and an axisymmetric profile of a cylindrical column is used as the computational domain. The bubble shape and the flow pattern around the bubble are relatively stable in case (a), and are oscillating in case (b). The oscillating phenomenon in case (b) is consistent with the experimental observations. Table 2 shows comparisons of the computational results to experimentally determined terminal rise velocities (Haberman and Morton, 1956), and the difference between them is less than 20%. Furthermore, to check the influence of the grid density on the simulation, two different grid systems (33×100 and 59×167) are used as shown in Table 2. It is shown that the difference of the grid systems is very small. Using the same numerical method, Hong et al. (1996) simulated the formation of a single-bubble chain

Table 2
Comparison of bubble rise velocities obtained by the numerical simulation with bubble rise velocities found in the literature

	Case (a)		Case (b)	
Liquid phase	Glycerin solution		Distilled water	
d_b (cm)	1.2	1.2	0.8	0.8
Grid system	33×100	59×167	33×100	59×167
Computational result of bubble rise velocity (cm/s)	20.23	19.28	19.81	19.32
Bubble rise velocity (cm/s) obtained from Haberman and Morton (1956)	23.6	23.6	23.0	23.0

Table 3
Comparison of drag coefficients for flow passing a sphere from the numerical simulation with drag coefficients found in the literature

	Condition 1	Condition 2	Condition 3
Liquid phase	Glycerin solution	Glycerin solution	Distilled water
Particle diameter (cm)	0.635	0.635	0.5
Liquid velocity (cm/s)	20	70	20
Reynolds number	29.0	101.3	1000
Predicted drag coefficient	1.29	0.87	0.55
Drag coefficient from White (1974)	2.17	1.18	0.60

and the bubble breakage due to a collision with a particle, and the simulation results agree closely with the experimental visualization.

To examine the accuracy of the code for predicting the force on the particle, the flow over a single sphere is simulated under three conditions as given in Table 3. Table 3 shows that the code predictions of drag coefficients are satisfactory under the moderate and high Reynolds numbers in comparison with empirical results by White (1974). However, a relatively large discrepancy is shown under the low Reynolds number. Mainly, the discrepancy is caused by the error the code suffers when calculating the frictional drag on the sphere surface using the velocity field.

4.2. Results and discussion

4.2.1. In distilled water

Fig. 7 shows the computational result and the analytical model prediction of F on a particle ($d_p = 0.5$ cm) during the collision with a bubble ($d_b = 0.8$ cm) in water. The Reynolds number based on particle size and bubble terminal velocity is 1000. The computed F has a high frequency oscillation component. The high frequency oscillation is due to the fluctuation of p_b. The magnitude and frequency of the oscillation of the predicted pressure inside the bubble is consistent with the experimental results from Vokurka (1990) and Jensen (1974). A similar air bubble oscillation was also reported by another VOF simulation (Barkhudarov and Chin, 1994).

The force, F, consists of three terms: (1) the pressure force, F_p, generated by the pressure distribution on the particle surface; (2) the friction force, F_f, originating from the shear stress on the particle surface induced by the viscous fluid flowing over the particle surface; and (3) the gravitational force. The simulation shows that during the entire collision period F_f is less than 10% of F_p; therefore, the viscous effect is insignificant. It should be noted that the size of the bubble and particle used in the experimental study are not equal to those used in the computation. In the experiment, d_p and d_b have to be larger than 0.95 and 1.2 cm, respectively, so that during the bubble–particle collision, F is large enough to generate an effective signal to noise ratio from the microforce balance. On the other hand, in the computation, there is a maximum bubble size that the present code can handle. For an air bubble of d_b larger than 0.8 cm in water, there is a continuous tiny bubble shedding in the simulation, which results in great difficulties in the convergence of solution. A qualitative comparison of Figs. 2 and 7

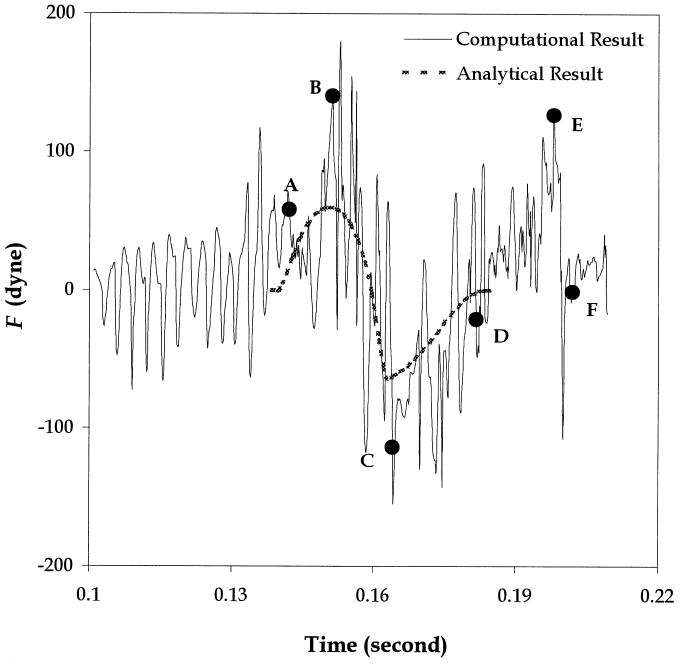

Fig. 7. Computational and analytical results of the force variation on a particle ($d_p = 0.5$ cm) during the collision with a bubble ($d_b = 0.8$ cm) in water.

shows that the F variation obtained by computation has the same overall shape as the experimental F variation over the entire collision process. Fig. 7 also shows that the analytical result of the force variation agrees well with the computational result in a real time sequence except the last stage of the collision, i.e. $t > 0.18$ s. The magnitude of the F variation predicted by the analytical model is smaller than that of the computational result because the analytical model neglects the bubble shape deformation and the liquid motion.

Fig. 8(a) to (f) shows the simulated liquid velocity distributions and the pressure contours around the particle at points A through F in Fig. 7. The liquid in front of the rising bubble is pushed upward which results in a building up of a liquid pressure in front of the bubble. As the bubble approaches the particle, the increased pressure zone and the upward fluid flow begin to exert an upward force on the bottom of the particle even before the contact is made. When the bubble contacts the bottom of the particle, the pressure at the bubble–particle contact area increases to the pressure of the bubble. As the size of the contact area increases, F continuously increases and reaches its maximum value at point B. From point B to C, the location of the high pressure contact area quickly shifts to the sides of the particle and eventually to the upper portion of the particle, which results in the maximum downward force at point C. From point C to D, the doughnut-shaped bubble recovers its shape. From point D to E, the bubble is elongated and still in touch with the particle. Because the bubble rises within the hydrostatic pressure field induced by the gravitational force, the pressure of the liquid surrounding the bubble and the pressure inside the bubble continuously decreases. Therefore, the pressure at the bubble–particle contact area quickly decreases. A low-pressure

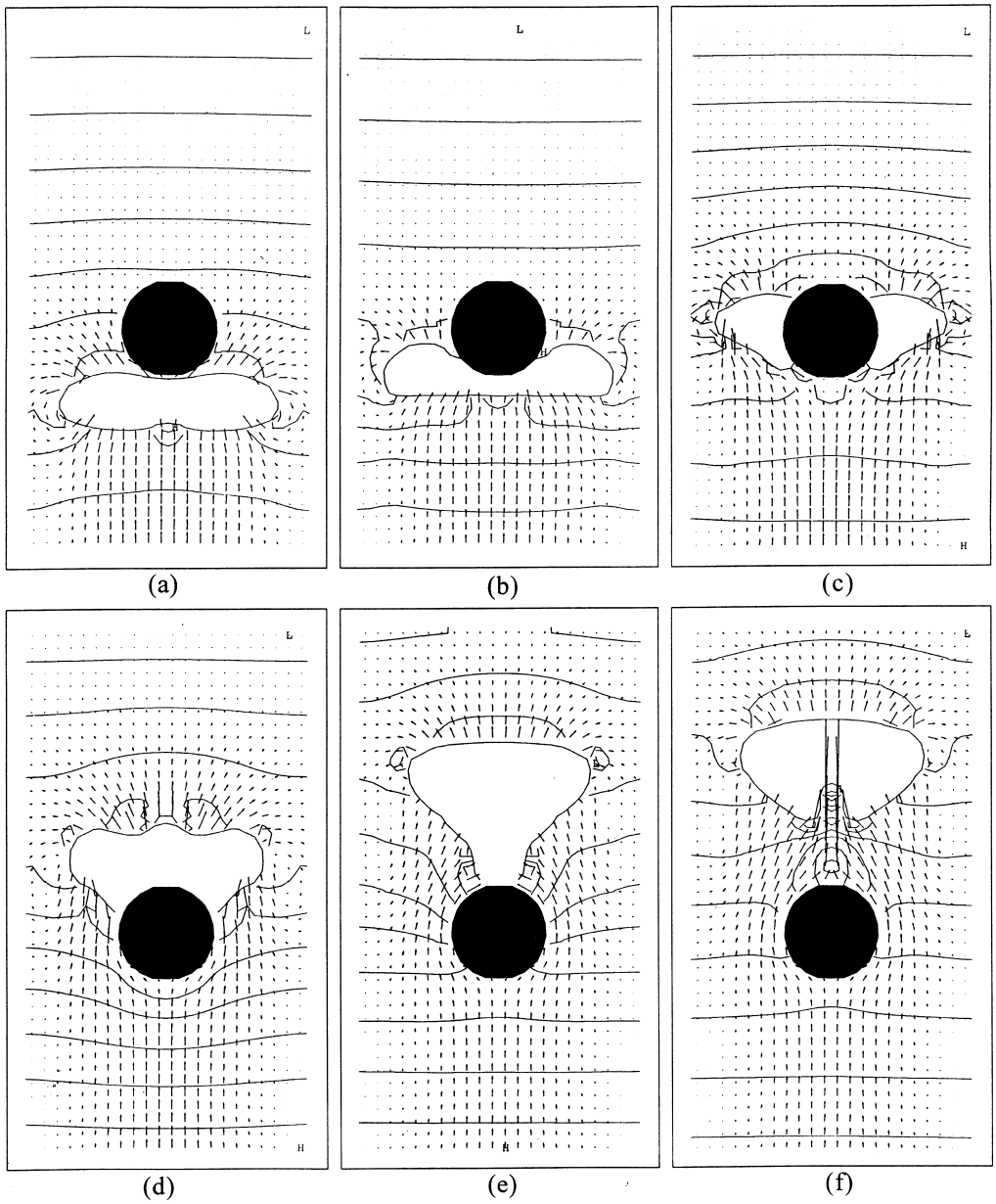

Fig. 8. Simulated liquid velocity distribution and pressure contours around the particle at points A through F in Fig. 7 (H and L represent high and low pressures, respectively).

zone is thus formed at the top of the particle, which produces an upward force on the particle. Consequently, F quickly increases to a local maximum, point E. After the bubble detaches from the particle, F drops back to zero. A sequence of experimental images of the collision process between a stationary particle ($d_p = 0.5$ cm) and a bubble ($d_b = 0.8$ cm) is shown in Fig. 9 that is consistent with the simulation results.

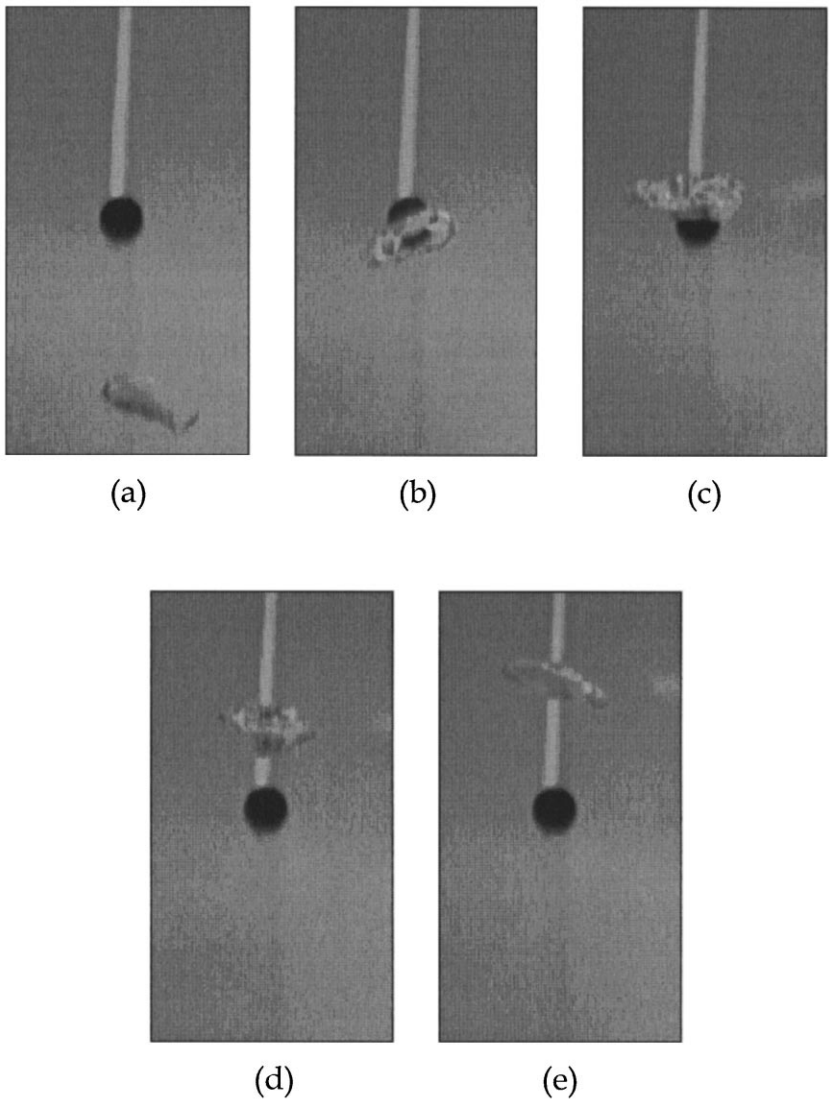

Fig. 9. Visualization of the collision sequence of a stationary particle ($d_p = 0.5$ cm) and a bubble ($d_b = 0.8$ cm) in water at: (a) $t = 0$; (b) $t = 0.0833$; (c) $t = 0.121$; (d) $t = 0.154$; and (e) $t = 0.179$ s.

4.2.2. In glycerin solution

4.2.2.1. Stationary particle. Fig. 10 shows the computational result for the F variation during the collision between a bubble ($d_b = 1.2$ cm) and a particle ($d_p = 0.5$ cm) in 80 wt% glycerin solution. The Reynolds number based on the particle size and the bubble terminal velocity is 22.8. Comparisons between Figs. 7 and 10 show that the pattern of the force variation is different in low and high viscous liquids, which is consistent with the experimental results in Figs. 2 and 3. A comparison of Figs. 3 and 10 shows that the computational result qualitatively agrees with the experimental result. However, the predicted maximum value of F is less than that of the

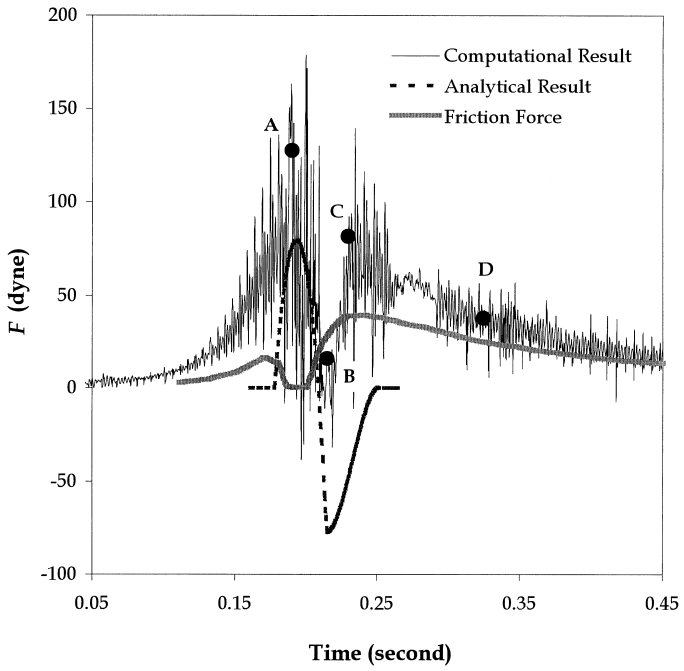

Fig. 10. Computational and analytical results of the force variation on a stationary particle ($d_p = 0.5$ cm) during the collision with a bubble ($d_b = 1.2$ cm) in 80 wt% glycerin solution.

experimental results. This deviation is mainly due to the calculation of the friction force, F_f, as discussed earlier. As in the case of water, the fluctuation of F is induced by the oscillation of p_b. Fig. 10 shows that there are two maxima in F during the collision; no downward force present; and the particle gains upward momentum overall. The predicted F variation from the analytical model follows that of the computation only in the early stage, and the maximum F obtained by the analytical model is lower than that from the computation. The major reason for the discrepancy is because the viscous force, which the analytical model does not count for, plays an important role in this case.

Fig. 11(a)–(d) presents the flow fields and the pressure distributions around the particle at points A through D in Fig. 10. As discussed for the case of water, when the bubble approaches the particle from below, the increased pressure zone and the liquid motion at the roof of bubble begin to produce an increasing upward force on the particle. Due to the high liquid viscosity, the upward liquid motion produces significant shear stress on the particle surface, which is much greater than that in the case of water. Therefore, there is a significant increase in F even before the bubble contacts the particle. This upward force gradually reaches a maximum value at point A. It is noted that when the bubble covers the bottom of the particle, F_f is greatly reduced because the shear stress becomes zero in the bubble–particle contact area. From point A to B, the bubble–particle contact area quickly shifts from the bottom of the particle to its side, which results in a sharp decrease of F down to a minimum around point B. After the particle penetrates the bubble, from point B to C, the area exposed to the bubble wake at the bottom of the particle increases. The upward liquid motion in the bubble wake

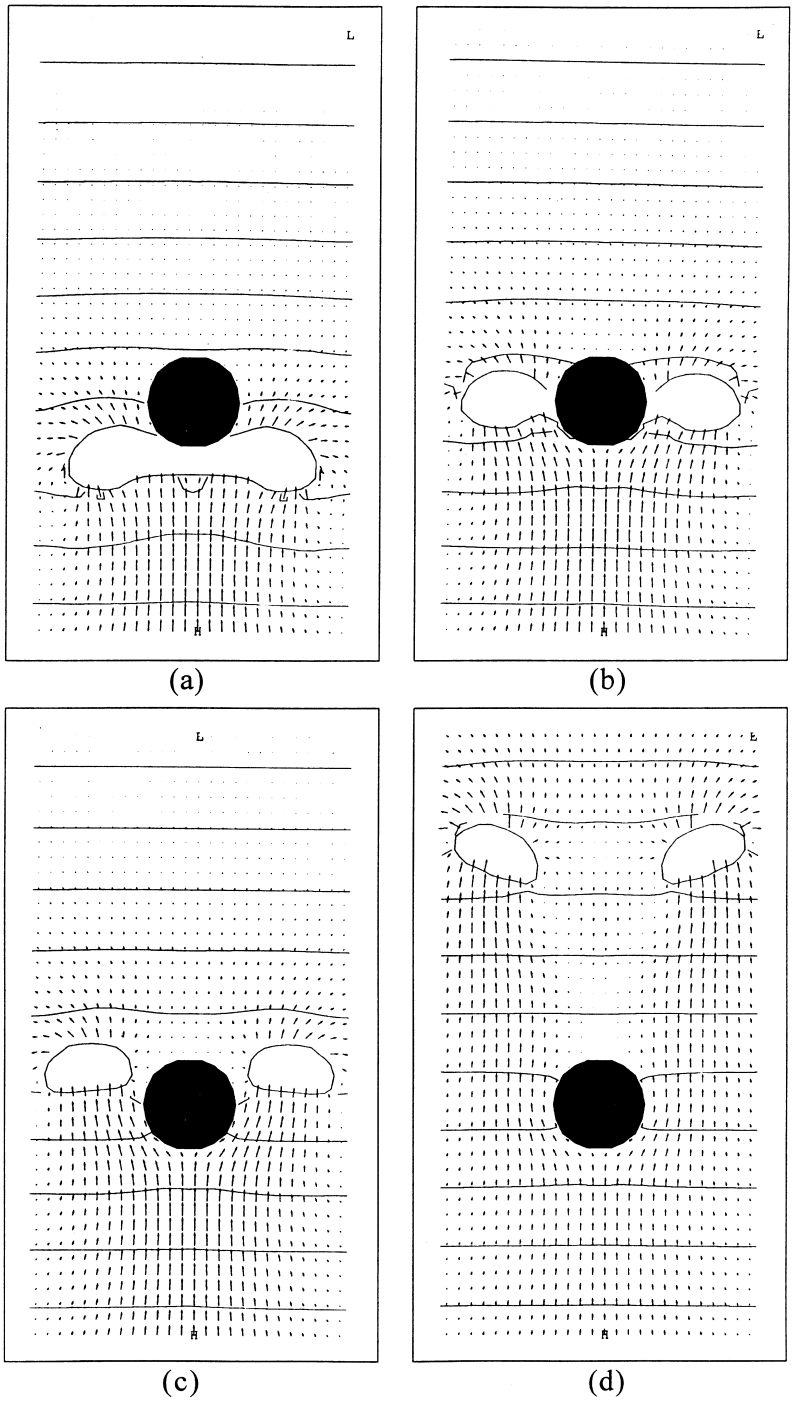

Fig. 11. Simulated liquid velocity distribution and pressure contours around the particle at points A through D in Fig. 10 (H and L represent high and low pressures, respectively).

creates an increasing upward shear stress force on the particle that overshadows the downward pressure force generated in the bubble–particle contact area. Thus, there is no negative F in the entire collision process. As the bubble rises, the surface area of the particle exposed to the bubble wake continuously increases until the entire particle is within the bubble wake at point C, where F reaches a local maximum. As the distance between the bubble and the particle increases, the intensity of the bubble wake around the particle decreases and F gradually decreases to zero. It is observed that the doughnut-shaped bubble detaches from the particle surface and keeps rising as doughnut-shape instead of reforming immediately as in the case of water. Compared to the case of water, the contact area of bubble and particle on the upper portion of the particle surface is greatly reduced, which leads to a much smaller downward force. There is no bubble–particle contact area on the top of the particle; therefore, the second peak of F is produced only by the wake of the bubble. Fig. 12 presents an experimental demonstration of the collision process between a stationary particle ($d_p = 0.5$ cm) and a bubble ($d_b = 1.2$ cm). The visualization agrees closely with the computational results shown in Fig. 11.

4.2.2.2. Moving particle. To obtain a further understanding of the bubble–particle interaction during the collision, a numerical simulation is conducted for the collision process of a rising bubble ($d_b = 1.2$ cm) with a falling particle ($d_p = 0.635$ cm). The particle is assumed to move downward along the central axis of the cylindrical column at a speed w_p of 50 cm/s. The Reynolds number based on the particle size and bubble–particle relative velocity is about 101. Because of the code limitation, the particle is assumed to move at a constant velocity w_p throughout the collision. The motion of the particle is simulated by fixing the particle in the computational domain and superimposing the liquid phase with a velocity, w_l, of 50 cm/s.

Fig. 13 shows the computational result of the force variation, and Fig. 14(a)–(e) shows the velocity field and the pressure distribution around the particle at points A through E. Differently from other cases, Fig. 13 shows a large decrease in F at the early stage of the collision. The pressure and the velocity distributions induced by the relative motion of the particle and the liquid exist before the collision occurs. The pressure and velocity fields generate an initial upward force, F_o, on the particle. A high pressure point ($p = p_o$) is located at the bottom of the particle and a high pressure zone surrounds this point. Meanwhile, a low-pressure zone exists around the top of the particle. F_o consists of two forces: a form drag force, F_p, produced by the high and the low pressure zone; and a friction drag force, F_f, induced by the high viscous liquid flowing over the particle surface at w_l.

When the bubble first touches the particle, the pressure at the bottom of the particle drops to p_b. Note that p_b is much lower than p_o. As a result, F_p suddenly decreases and consequently F decreases drastically. Because p_b decreases as the bubble rises, the pressure around the bottom of the particle continuously decreases. Meanwhile, F_f also decreases as the contact area, where the shear stress is zero, increases. As a combined result, F reaches a minimum at point B. After the particle penetrates the bubble, the bottom of the particle is exposed to the wake of the bubble. The pressure at the bottom of the particle quickly recovers, and thus F increases. As the bubble separates from the particle, the entire particle falls within the bubble wake where the upward liquid velocity is higher than w_l. Both F_f and F_p, and therefore F, reach maxima as shown at point C. Since the distance between the moving particle and the

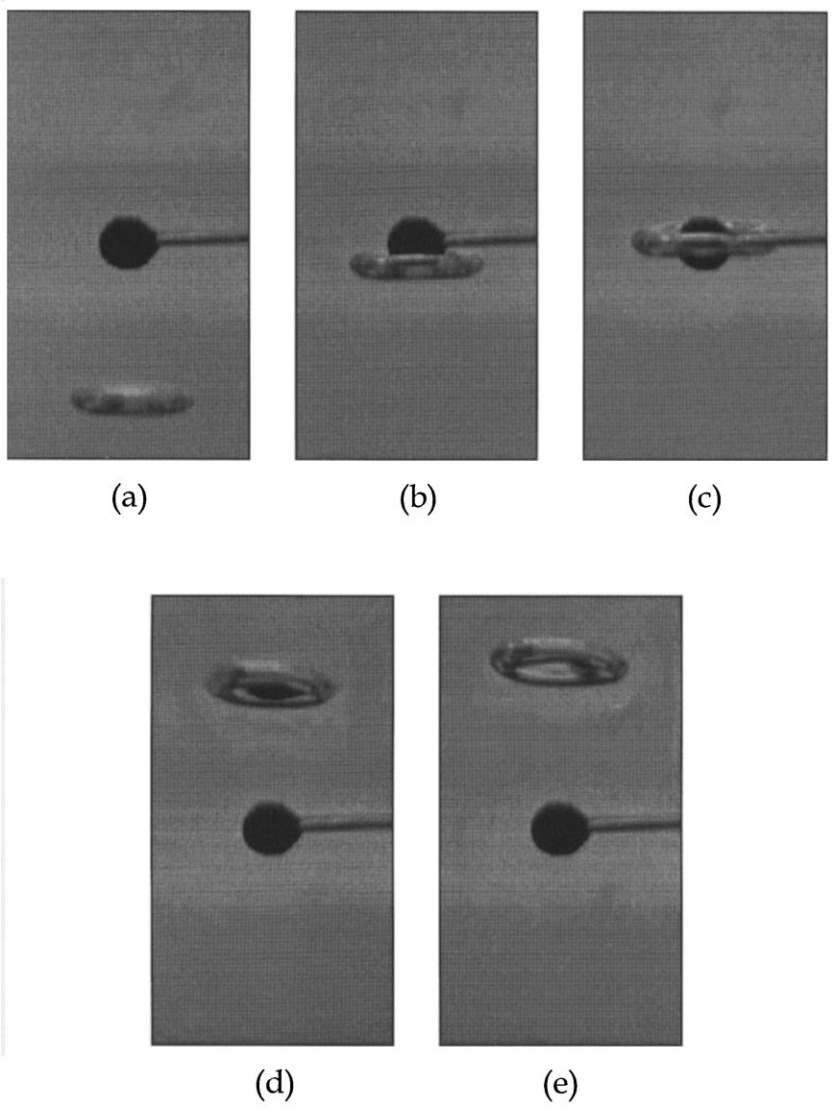

Fig. 12. Visualization of the collision sequence of a stationary particle ($d_p = 0.5$ cm) and a bubble ($d_b = 1.2$ cm) in 80 wt% glycerin solution at: (a) $t = 0$; (b) $t = 0.0708$; (c) $t = 0.0875$; (d) $t = 0.150$; and (e) $t = 0.158$ s.

bubble increases rapidly after separation, the influence of the bubble wake dissipates quickly, and therefore, F quickly decreases to its initial value.

In Fig. 13, the fluctuation of F is again the result of the oscillation of p_b. After the particle penetrates the bubble, there is a strong shear layer flow around the inside edge of the bubble, which results in the elongation of the bubble and generates a series of tiny bubbles as seen in Fig. 14(d). Each tiny bubble separation results a large oscillation of p_b. The oscillation causes the large magnitude high frequency fluctuations of F at the last stage of the collision process. Based on the force variation of Fig. 13, it can be obtained with a steel ball that the downward velocity of the particle is reduced by 3.6% after the collision.

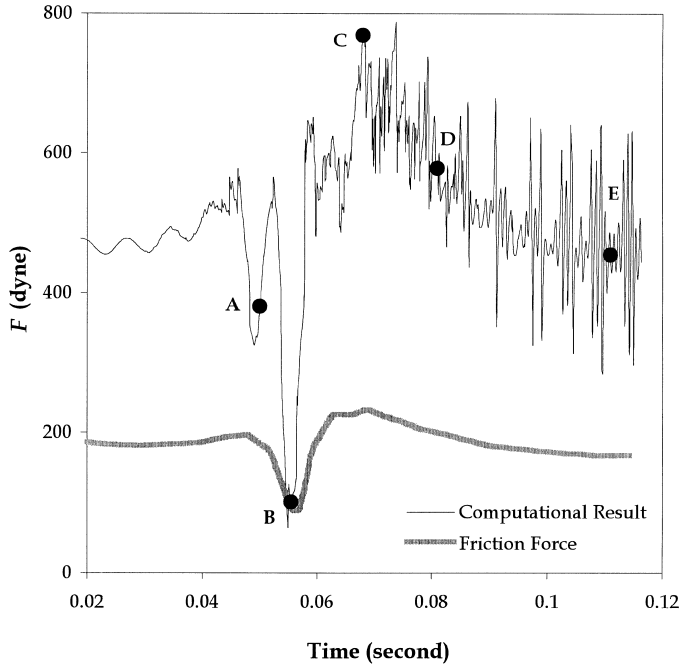

Fig. 13. Computational result of the force variation on the moving particle ($d_p = 0.635$ cm, $w_p = 50$ cm/s) during the collision with a bubble ($d_b = 1.2$ cm) in 80 wt% glycerin solution.

Because of the limitation of the force measuring system, F is not measured experimentally on the moving particle. Fig. 15 shows experimental images of the bubble–particle collision process in 80 wt% glycerin solution, and the figure agrees closely with the simulation result of the dual movement collision sequence shown in Fig. 14.

5. Concluding remarks

The force variation on a particle during a bubble–particle collision is measured experimentally. An analytical model is developed to account for the bubble pressure effects during the collision. Furthermore, numerical simulations are conducted under three conditions. The predictions agree well with the experimental observations. The computational results provide detailed velocity fields and pressure distributions around the bubble and the particle as well as velocity and pressure variations with respect to time over the entire collision process.

When a bubble collides with a stationary particle, the force on the particle first increases, then decreases, and again increases. The magnitude of the force variation is comparable to the product of the difference of the hydrostatic pressure based on the bubble height and the cross-sectional area of the particle. If the collision takes place in water, the pressure force predominates and the viscous force can be neglected. The particle experiences both upward and downward forces during the collision process. On the other hand, if the collision takes place in

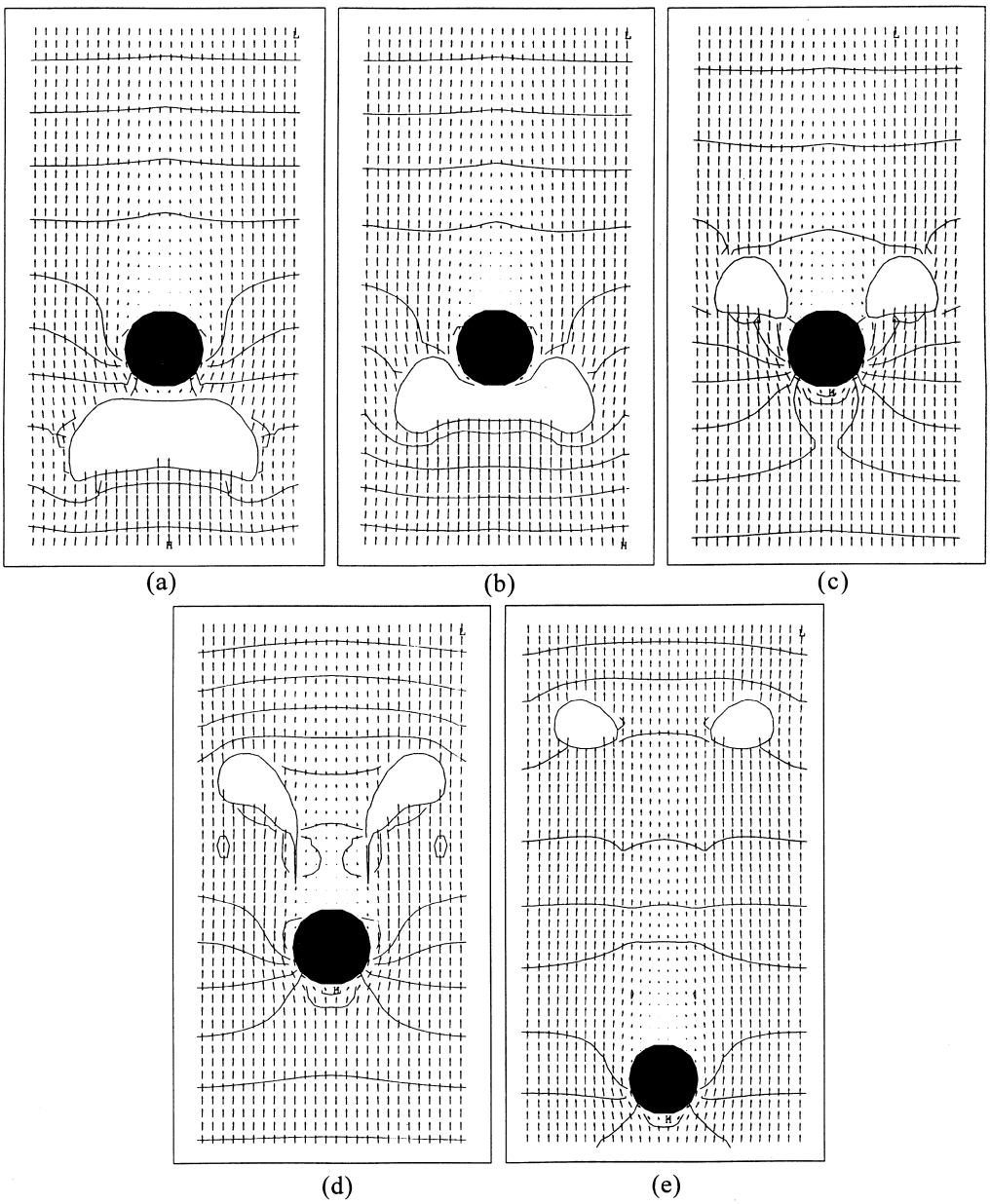

Fig. 14. Simulated liquid velocity distribution and pressure contours around the moving particle at points A through E in Fig. 13 (H and L represent high and low pressures, respectively).

80 wt% glycerin solution, both the pressure force and the viscous force predominate and the force on the particle is upward throughout the collision.

When a bubble collides with a falling particle, the particle experiences an initial upward force before the collision. If the speed of the particle is relatively large compared with the

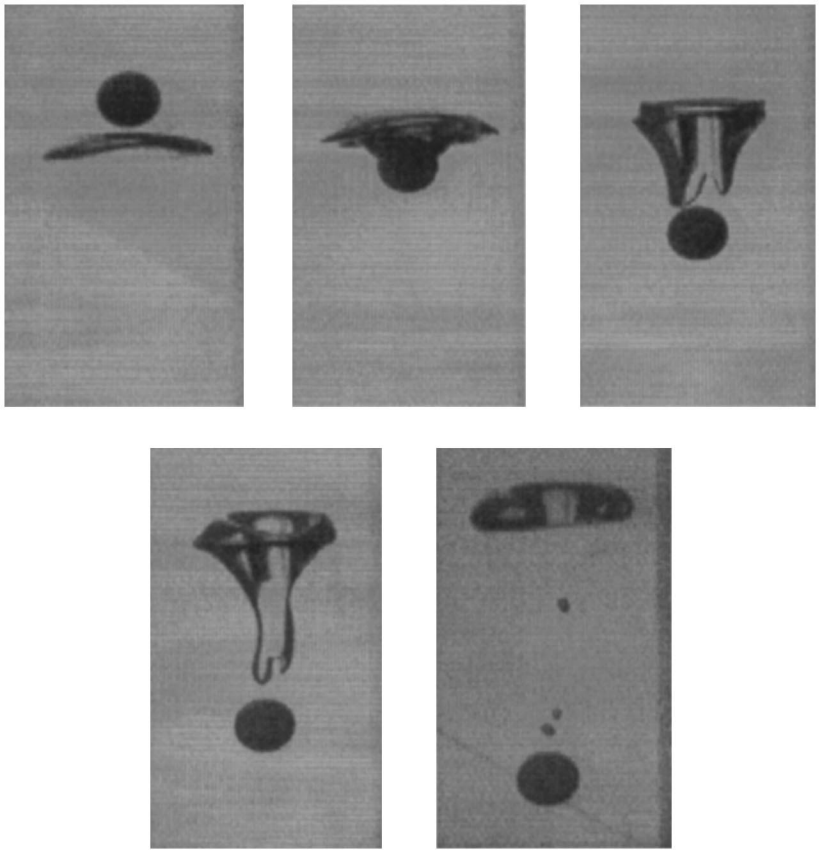

Fig. 15. Visualization of the collision sequence of a copper sphere ($d_p = 1.22$ cm) and a spherical-cap air bubble ($d_b = 1.97$ cm) in 80 wt% glycerin solution (time interval between each picture = 1/60 s).

bubble rise velocity, there is a great decrease in the upward force on the particle in the early stage of the collision, followed by a quick recovery and a significant increase in the upward force due to the pressure and the wake effect of the bubble. The magnitude of the force variation is of the same order as the drag force on the particle before collision.

Acknowledgements

The authors thank Dr. S.-C. Liang for her valuable comments and suggestions. This work was sponsored, in part, by the Ohio Super Computer Center and NSF grant CTS-9528380.

References

Barkhudarov, M.R., Chin, S.B., 1994. Stability of a numerical algorithm for gas bubble modelling. Int. J. Numer. Meth. Fluids 19, 415–437.

Bruce, P.N., Revel-Chion, L., 1974. Bed porosity in three-phase fluidization. Powder Technol. 10, 243–249.

Bugg, J.D., Rowe, R.D., 1993. Modeling large-bubble formation at submerged orifices. Int. J. Numer. Meth. Fluids 16, 813–825.

Butt, H.-J., 1994. A technique for measuring the force between a colloidal particle in water and a bubble. J. Coll. Interf. Sci. 166, 109–117.

Chapman, R.B., Plesset, M.S., 1971. Thermal effects in the free oscillation of gas bubbles. J. Basic. Engng Trans. ASME, Series D 93 (3), 373–376.

Chen, Y.-M., Fan, L.-S., 1989a. Bubble breakage mechanisms due to collision with a particle in a liquid medium. Chem. Eng. Sci. 44, 117–132.

Chen, Y.-M., Fan, L.-S., 1989b. Bubble breakage due to particle collision in a liquid medium: particle wettability effects. Chem. Eng. Sci. 44, 2762–2767.

Deitz, D., 1998. Connecting the dots with CFD. Mechanical Engineering 120 (3), 90–91.

Ducker, W.A., Cook, R.F., Clarke, D.R., 1990. Force measurement using an AC atomic force microscope. J. Appl. Phys. 67, 4045–4052.

Elliott, G.E.P., Riddiford, A.C., 1967. Dynamic contact angles. J. Colloid Interf. Sci. 23, 389–398.

Fan, L.-S., 1989. Gas–Liquid–Solid Fluidization Engineering. Butterworths, Stoneham.

Fan, L.-S., Tsuchiya, K., 1990. Bubble wake dynamics in liquids and liquid–solid suspensions. Butterworth, Stoneham.

Garcia-Briones, M.A., Brodkey, R.S., Chalmers, J.J., 1994. Computer simulations of the rupture of a gas bubble at a gas-liquid interface and its implications in animal cell damage. Chem. Eng. Sci. 49, 2301–2320.

Haberman, W.L., Morton, R.K., 1956. An experimental study of bubbles moving in liquids. Trans. Amer. Soc. Civil Eng. 121, 227–250.

Harper, R.P., Hirt, C.W., Sicilian, J.M., 1991. Flow-3D: computational modeling power for scientists and engineers, FSI-91-00-1. Flow Science, Inc. report.

Henriksen, H.K., Ostergaard, K., 1974. On the mechanism of break-up of large bubbles in liquids and three-phase fluidised beds. Chem. Eng. Sci. 29, 626–629.

Hirt, C.W., Nichols, B.D., 1981. Volume of fluid (VOF) method for the dynamics of free boundaries. J. Comp. Phys. 39, 201–225.

Hirt, C.W., Nichols, B.D., Romero, N.C. 1975. SOLA—a numerical solution algorithm for transient fluid flow. Los Alamos Scientific Laboratory Report. LA-5852.

Hong, T., Zhu, C., Fan, L.-S., 1996. Numerical modeling of formation of single bubble chain and bubble breakage due to collision with particle in liquids. Proceedings of the Fluids Engineering Division Summer Meeting, San Diego. ASME, FED-Vol (236), 581–588.

Jensen, F.B., 1974. Shock-excited pulsations of large air bubbles in water. J. Fluids Engng, Trans. ASME 96, 389–393.

Kumar, S., Kusakabe, K., Raghunathan, K., Fan, L.-S., 1992. Mechanism of heat transfer in bubbly liquid and liquid-solid systems: single bubble injection. AIChE J. 38, 733–741.

Lee, J.C., 1965. Discussion in the paper of Adlington and Thomson. Proc. 3rd Eur. Symp. Chem. React. Engng. Pergamon Press, Oxford, p. 211.

Lee, J.C., Sherrad, A.J., Buckley, P.S., 1974. Optimum particle size in three phase fluidized bed reactors. In: H. Angelino et al. (Ed.). Fluidization and its Application. Cepadues-Editions, Toulouse, p. 407.

Lin, X.-Y., Creuzet, F., Arribart, H., 1993. Atomic force microscopy for local characterization of surface acid-base properties. J. Phys. Chem. 97, 7272–7276.

Muroyama, K., Fan, L.-S., 1985. Fundamentals of gas-liquid-solid fluidization. AIChE J. 31, 1–34.

Ostergaard, K., 1966. On the growth of air bubbles formed at a single orifice in a water fluidized bed. Chem. Eng. Sci. 21, 470–472.

Tomiyama, A., Sou, A., Minagawa, H., Sakaguchi, T., 1993. Numerical analysis of a single bubble by VOF method. JSME J., Series B 36, No. 1.

Tsao, Y.-H., Evans, D.F., Wennerstrom, H., 1993. Long-range attractive force between hydrophobic surfaces observed by atomic force microscopy. Science 262, 547–550.

Vakhrushev, I.A., Efremov, G.I., 1970. Chem Technol Fuels Oils. (USSR), 5/6. Cited by Fan and Tsuchiya (1990), p. 376.

Vokurka, K., 1990. Amplitudes of free bubble oscillations in liquids. J. Sound Vibrat. 141, 259–275.

White, F.M., 1974. Viscous Fluid Flow. McGraw-Hill, New York.

Zhu, C., Liang, S.-C., Fan, L.-S., 1994. Particle wake effects on the drag force of an interactive particle. Int. J. Multiphase Flow 20, 117–129.